Induced Roll Computations for Conventional Missiles

F. J. Priolo* and A. B. Wardlaw Jr.†
Naval Surface Warfare Center, White Oak, Silver Spring, Maryland 20903

The ZEUS program, which solves Euler's equations by spatial marching, is applied to conventional missiles characterized by circular cross-sectional bodies, canard control surfaces, and a cruciform tail. ZEUS incorporates a multiple-zone gridding technique and a second-order extension of Godunov's method. The Godunov method is an upwind scheme based on the Riemann problem for steady supersonic flow and cast in a control volume form. Second-order accuracy is obtained by computing local slopes and adding a predictor step. The scheme fits the bow shock and captures imbedded shocks. The ZEUS code is applied to two canard-controlled missiles with cruciform tails to predict longitudinal and lateral-directional (e.g., induced rolling moment) aerodynamic characteristics.

Nomenclature

A^k = area of control volume edge lying in the $z = z^k$ plane
C_l = rolling moment coefficient, rolling moment/$q_\infty Sd$
C_M = pitching moment coefficient, pitching moment/$q_\infty SL$
C_N = normal force coefficient, normal force/$q_\infty S$
C_Y = side force coefficient, side force/$q_\infty S$
d = diameter
F = flux vector, Eq. (1)
H_0 = stagnation enthalpy
L = reference length, length of configuration
M_∞ = freestream Mach number
n = vector normal to cell edge, Eq. (1), $= (n_x, n_y, n_z)$
$|n|$ = cell edge area
p = pressure
q_∞ = freestream dynamic pressure
$R_\pm$ = upper and lower supersonic streams for the Riemann problem, Fig. 3
S = reference area, maximum cross-sectional area of the body
U = flux vector, Eq. (1)
(u,v,w) = Cartesian velocity components
(x,y,z) = Cartesian coordinates with z along the missile axis
α = angle of attack, deg
δ = canard deflection angle, positive with leading edge up, Figs. 7, 8, 11–13
δ_f = flow direction angle, Fig. 3
γ = ratio of specific heats
κ' = difference limiter, Eq. (3)
ϕ = crossflow plane roll angle measured clockwise from the positive x axis
ρ = density

Subscripts

n,m,k = cell center, Fig. 4
∞ = ambient conditions
1,2,3,4 = canard panel numbers as defined in Figs. 6 and 10 (Figs. 8, 11–13)

Presented as Paper 89-0331 at the AIAA 27th Aerospace Sciences Meeting, Reno, NV, Jan. 9–12, 1989; revision received Dec. 19, 1989.

*Aerospace Engineer, Applied Mathematics Branch. Member AIAA.
†Aerospace Engineer, Applied Mathematics Branch. Associate Fellow AIAA.

I. Introduction

TRADITIONALLY, missile aerodynamics has been predicted using slender body theory, linear theory, and semi-empirical methods that are based on an extensive data base. These methods determine the global aerodynamic characteristics using a minimum of computational resources. Numerical methods, on the other hand, are independent of experimental data but require a greater computational effort. Such techniques are applicable to a wider range of configurations and flight parameters and provide detailed flowfield properties not attainable using empirical methods. A number of numerical procedures have been applied to missiles, including linearized potential, panel, nonlinear full potential, space marching Euler, time marching Euler, parabolized Navier-Stokes, thin-layer Navier-Stokes, and Reynolds-averaged Navier-Stokes. A survey of these methods is provided by Hoeijmakers.[1]

The present paper focuses on applying the Euler equations to missiles in supersonic flight. Under these conditions, the Euler equations are hyperbolic, and the missile's flowfield can be determined from known flow conditions at a cross-sectional plane near the nose tip. This initial data plane, which is generated by a sharp cone or blunt body starting program, is marched down the length of the missile to the base, as shown in Fig. 1. Computational times for a complete missile are similar to those for linear potential methods given by Ref. 1 (approximately 1–5 min of Cray time). However, the Euler equations can treat shocks of arbitrary strength and convect vorticity, whereas potential methods cannot. Vorticity generated by separation is not described by the Euler equations, and phenomena such as body vortices must be empirically modeled.

Space marching Euler methods were originally applied to re-entry vehicles that featured conical geometries complicated by cuts and flaps. Mesh generation was accomplished using a single transformation,[2–5] a technique that is not well suited to tactical missiles that are characterized by thin, low-aspect-ratio fins with sharp edges.

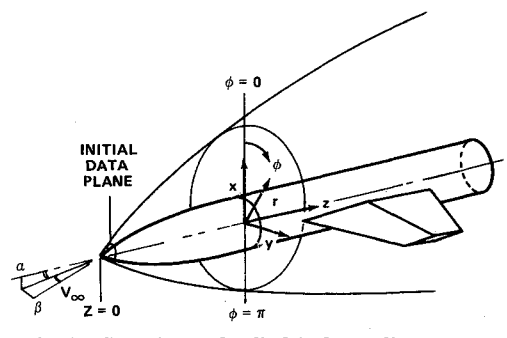

Fig. 1 Cartesian and cylindrical coordinate system.

Solutions for tactical missiles have been accomplished using a multiple zone gridding strategy. Initial work by Wardlaw et al.[6-10] applied the MacCormack scheme with characteristic boundary conditions. These characteristic boundary conditions were enforced at wing edges and surface discontinuities in conjunction with special procedures that applied oblique shocks and expansions where appropriate. These methods have been successfully applied to missiles but are not robust. For complex shapes, artificial viscosity and special procedures were adjusted on a trial and error basis. Additionally, Wardlaw et al.[11] combined the same multiple zone approach with Godunov's first-order method[12] for steady supersonic flow. Unlike the MacCormack approach, this technique was robust and devoid of any special procedures.

The Zonal Euler Solver (ZEUS) of Wardlaw et al.[13-16] is a space marching method that combines a simple multiple-zone gridding technique and a second-order extension of Godunov's method. The Godunov method is an upwind scheme based on the Riemann problem for steady supersonic flow. It is cast in control volume form and consists of a predictor and corrector step. The predictor step advances the primitive variables using Euler's equations in nonconservation form. Derivatives are computed using a limited central differencing procedure. The corrector step modifies Godunov's method by assuming linear property variations within each control volume. This program is devoid of explicit artificial viscosity and is robust. However, as in all space marching Euler solutions, the flow must remain supersonic in the axial direction. This effectively limits these solutions to the range in incidence and Mach number shown in Fig. 2.

The prediction of the lateral-directional aerodynamic characteristics of a missile is a very difficult test for any prediction method. As discussed by Lesieutre et al.,[17] tail loading is strongly influenced by canard trailing vorticity and afterbody vortices. In particular, for canard-controlled missiles with roll or yaw controlled canard deflections, an induced roll develops as a result of an asymmetric flowfield near the tail.

The current paper applies the ZEUS program to conventional missiles with circular bodies, canard control surfaces, and a cruciform tail.[18,19] Predictions are made of both the longitudinal and lateral-directional aerodynamic characteristics, and results are compared with experiment. A brief description of the ZEUS computational algorithm is provided in Sec. II. Section III discusses results, and Sec. IV outlines conclusions to be drawn from this study.

II. Computational Procedure

A. Zone Structure

The ZEUS program uses a multiple zone structure that provides a convenient framework from which to compute shapes having sharp edged fins. The crossflow plane is divided into several quadrilateral zones, and a simple separate transformation is applied to each. Zone boundaries are taken to coincide with the body, canard and tail surfaces, and with the bow shock, allowing fin thickness and fin deflections to be accurately modeled.

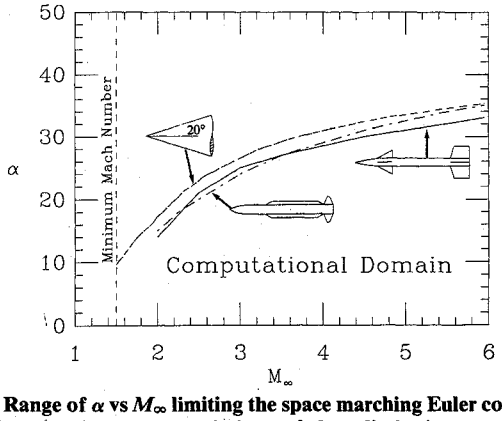

Fig. 2 Range of α vs M_∞ limiting the space marching Euler computational domain. As shown, variations of these limitations can occur, depending on the configuration.

B. Numerical Scheme

For steady supersonic flow, the Riemann problem represents the confluence of two two-dimensional supersonic streams, as illustrated in Fig. 3. At the point of intersection, shocks or expansion fans form that turn both streams to a common direction. The two final streams need not feature the same density or velocity and a slip line generally forms between them. The solution begins by guessing the slip line orientation and computing the pressure on each side. Since the shock and expansion relations are nonlinear, an iterative procedure is adopted that adjusts the slip line orientation until the appropriate direction is found. This direction is the one producing the same pressure in both streams. If the two streams forming the Riemann problem have similar properties, a closed form linear solution can be obtained. Alternatively, an approximate Riemann problem[20] can be constructed that has a closed form solution.

Using the notation of Fig. 4, mass and momentum conservation through a control volume can be expressed as

$$U^{k+1}_{n,m} = U^{k}_{n,m} - F_{n+\frac{1}{2},m} + F_{n-\frac{1}{2},m} - F_{n,m+\frac{1}{2}} + F_{n,m-\frac{1}{2}} \quad \text{(1a)}$$

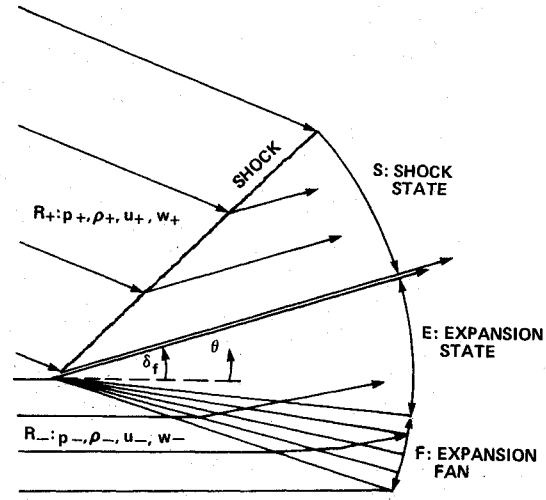

Fig. 3 Supersonic Riemann problem consists of two intersecting supersonic streams, R_+ and R_-.

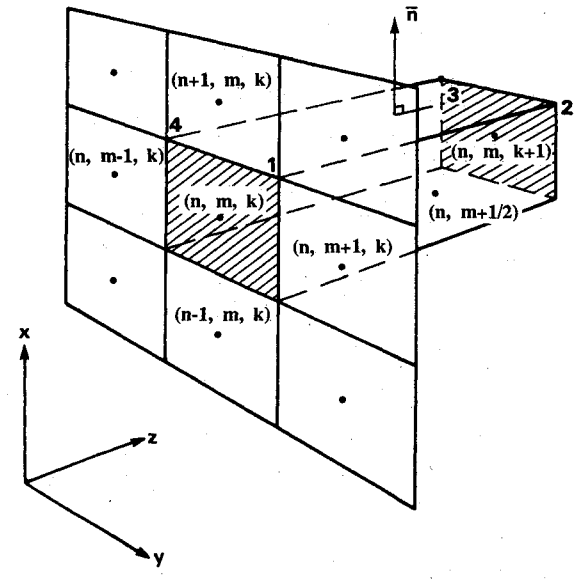

Fig. 4 Control volume nomenclature.

where

$$U^k_{n,m} = A^k_{n,m} \begin{bmatrix} \rho w \\ \rho w^2 + p \\ \rho wu \\ \rho wv \end{bmatrix}_{n,m}, \quad F_{n+\frac{1}{2},m} = \begin{bmatrix} \rho V \\ \rho wV + n_z p \\ \rho uV + n_x p \\ \rho vV + n_y p \end{bmatrix}_{n+\frac{1}{2},m}$$

$$V = n_{n+\frac{1}{2},m} \cdot (u, v, w)_{n+\frac{1}{2},m} \tag{1b}$$

Here, U is the flux in the z direction that passes through the shaded cell ends, whereas the F's are the fluxes associated with the remaining cell edges. Equations (1) are closed using the constant total enthalpy condition and the perfect-gas equation of state that yield the constraint

$$(p/\rho)[\gamma/(\gamma - 1)] + \tfrac{1}{2}(u^2 + v^2 + w^2) = H_0 \tag{2}$$

The ZEUS code integrates Euler's equations using a second-order Godunov method. Godunov's original method[12] (applied in Ref. 11) is first-order accurate and usually cast in a control volume form. Properties within each cell are assumed constant, and fluxes [F appearing in Eq. (1)] at cell edges are calculated using the Riemann problem. The two sets of properties adjacent to each cell edge define the two streams making up the Riemann problem. Fluxes crossing a cell edge are computed from the solution to the Riemann problem. Along any ray originating from the point of the initial stream intersection, properties are constant. The properties along the ray parallel to the cell edge are used to compute the flux. When this direction falls between the shocks/expansions defining the Riemann problem (see Fig. 3), the computed flux is influenced by properties at both adjacent cell edges. In other circumstances, when the flow normal to the cell edge is supersonic, the cell edge flux will be a function of only one cell's properties. The active cell is upstream or upwind of the cell edge, thus reflecting the correct domain of dependence of the problem.

Godunov's method is extended to second-order accuracy by adding a predictor step to determine properties at $z^k + \Delta z/2$ and linearly extrapolating these properties to the cell edge. The property slopes for both the predictor step and the linear extrapolation are computed using limited differences that prevent oscillations near shocks. These differences are calculated in the following manner:

$$\frac{\partial f}{\partial \xi} = \begin{cases} 0 & \text{if } c_1 < 0 \\ c_2 & \text{if } c_1 \geq 0 \end{cases} \tag{3}$$

where

$$c_1 = (f_{n+1,m} - f_{n,m})(f_{n,m} - f_{n-1,m}) \tag{4}$$

$$c_2 = \frac{\text{sign}(f_{n+1,m} - f_{n,m})}{\Delta \xi} \min \left\{ \begin{matrix} \dfrac{|(f_{n+1,m} - f_{n-1,m})|}{2} \\ \kappa' |f_{n+1,m} - f_{n,m}| \\ \kappa' |f_{n,m} - f_{n-1,m}| \end{matrix} \right\} \tag{5}$$

Here, f is some dependent variable differentiated with respect to some independent variable ξ and $1 \leq \kappa' < 2$.

The predictor step advances primitive variables using Euler's equations in nonconservation form. Near shocks and other discontinuities, the limiter reduces all slopes to zero and the scheme collapses to the first-order Godunov's method.

C. Boundary Conditions

ZEUS is based on a finite-volume formulation. Therefore, grid points do not lie on the boundary, but rather the cells adjacent to the wall have an edge lying along the boundary. Properties along cell edges adjacent to the wall are computed by extrapolating predicted properties to the wall using the cell slope normal to the wall. These edge properties do not satisfy the tangent flow boundary conditions and must be turned, using either an oblique shock or Prandtl-Meyer expansion to satisfy the wall boundary conditions. The flow is tangent to the wall, and only the post-turn pressure influences the flux at the edge lying on the wall.

Lifting surfaces may form and disappear as the solution is marched down the length of the missile. Cell edges that are partially covered by a surface are divided into two elements, one containing the edge area adjacent to the surface and the other containing the edge area adjoining another cell. Separate estimates of the fluxes acting on each element are added to determine the total edge flux.

The outer zone boundary is determined by tracking the domain of dependence of the numerical solution, using information contained in the Riemann problem.

D. Special Procedures

Artificial viscosity and other special procedures are not required by the ZEUS code. However, free parameters do occur in the difference limiters. In the program, κ' of Eq. (5) is set to 0 at cells next to fin surfaces, 1 at interior cells, and 2 at boundary cells in smooth flow regions. These values of κ' do not require adjustment from one problem to the next.

III. Results and Discussion

A. Computed Results

The ZEUS code has been applied to two conventional missiles with circular cross-sectional bodies, canard control surfaces, and a cruciform tail. Comparisons are made with the measured aerodynamic performance of each missile. Computations for the ZEUS code were performed on the SUN3 work station. Results were achieved using a marching step size of 90% of the CFL limit. A uniform mesh size of 72 × 144 (i.e., 72 points in the radial direction) was used for the complete 360-deg configuration. Computations featuring canards or tail fins were run using multiple zones. The approximate Riemann solver of Ref. 20 was employed for all of the computations.

Computations were performed on the canard-body-tail configuration shown in Fig. 5 and found in Ref. 18. This missile is characterized by a 2.25 caliber tangent ogive nose, a 7.6 caliber forebody, cruciform canards, a 5.6 caliber afterbody, and a cruciform tail in line with the canards. The roll orientation of the missile was $\phi = 45$ deg. Solutions were computed for an incidence range of 0–18 deg for Mach 2.35 and 0–30 deg for Mach 4.6. Above these angles of attack, the flow became subsonic in the axial direction near the fin leading edge, and the space marching procedure could not be continued.

Calculated and measured longitudinal loads as a function of angle of attack are illustrated in Fig. 6 for the configuration of Fig. 5 without canard deflection. ZEUS predictions agree reasonably well with experimental results. Nonlinearities in the C_M vs α curves are due to the influence of body and canard vortices. These vortices pass close to the tail at intermediate incidences (i.e., 10 deg $\leq \alpha \leq$ 20 deg). This reduces tail effectiveness and leads to a flattening of the C_M vs α curve.

Figure 7 shows the lateral-directional load comparisons for the same shape with canards 2 and 4 deflected asymmetrically 10 deg. The computed lateral-directional loads, which compare favorably with measured data, result from the asymmetric curved crossflow shocks and ensuing vortices generated by the canards which are deflected in opposite directions. At high incidences, asymmetric crossflow shocks also appear on the afterbody adding asymmetries into the flowfield that is convected downstream. Experimentally, the missile features vortices shed from the canards and afterbody, the latter as a consequence of boundary-layer separation.

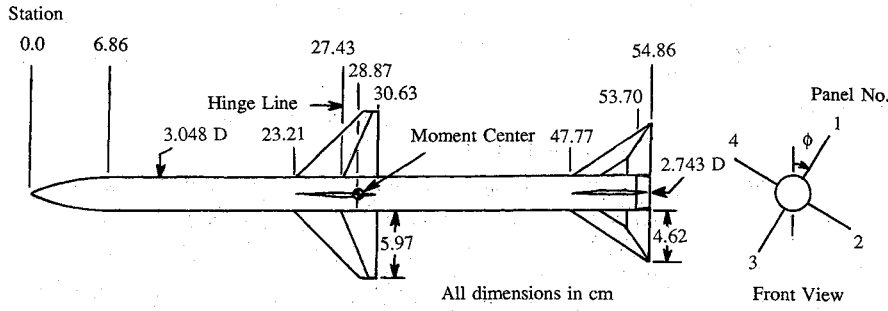

Fig. 5 Canard-body-tail configuration.[18]

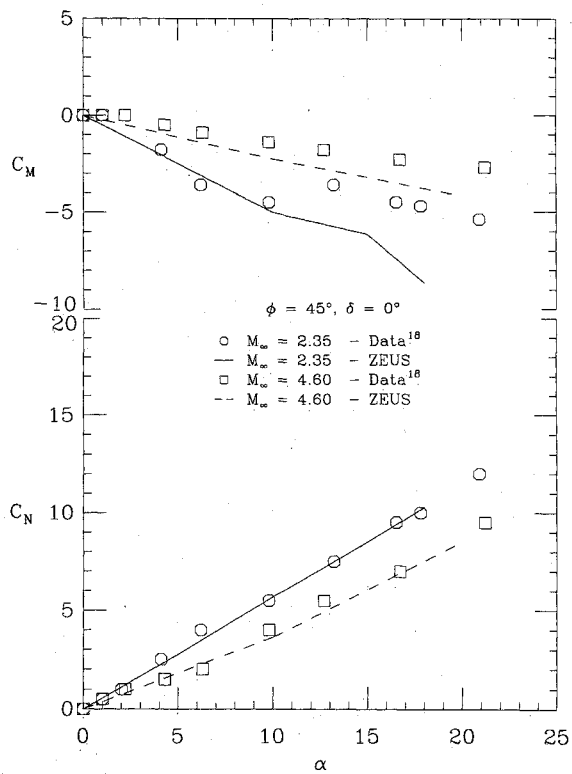

Fig. 6 Computed and measured C_N vs α and C_M vs α for the configuration of Fig. 6 without canard deflection for $\phi = 45$ deg at $M_\infty = 2.35$ and 4.6.

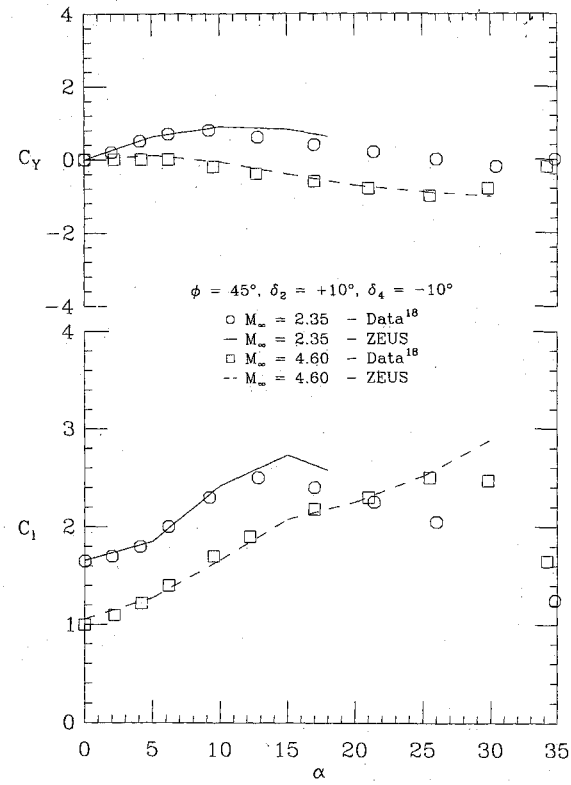

Fig. 7 Computed and measured C_l vs α and C_Y vs α for the configuration of Fig. 6 with canards 2 and 4 deflected asymmetrically 10 deg for $\phi = 45$ deg at $M_\infty = 2.35$ and 4.6.

Computed pressures and axial vorticity contours at the canard trailing edge are displayed in Fig. 8 for Mach 4.6 at 25-deg incidence, with canards 2 and 4 deflected asymmetrically 10 deg. Visible are the asymmetric shock structures and vortices. This flowfield is convected over the tail affecting the rolling moment, as shown in Fig. 7. Also shown is the interaction of the bow shock with the windward fins.

Computations were also performed on the canard-body-tail configuration of Ref. 19, which is illustrated in Fig. 9. This missile is characterized by a 2.25 caliber tangent ogive nose on a 3.7 caliber forebody, cruciform canards, a 12.7 caliber afterbody, and a cruciform tail in line with the canards. Solutions were calculated for an incidence range of 0–20 deg, a Mach number of 2.5, and missile roll orientations of $\phi = 0$, 26.6, and 45 deg. The flow became subsonic in the marching direction at higher angles and attack, and the space marching procedure could not be continued.

Calculated and measured normal force and pitching moment as a function of angle of attack are displayed in Fig. 10 for the configuration of Fig. 9. Results are shown in Fig. 10 at $\phi = 0$ deg with and without canard deflection and at $\phi = 45$ deg without canard deflection. Computations were performed for incidences up to 18 deg, the extent of the experimental data. Predicted and measured longitudinal loads are in good agreement.

The rolling moment and side force comparisons, for the same configuration, are illustrated in Figs. 11 and 12 for the three roll orientations, with canards 2 and 4 asymmetrically deflected 5 deg. Here, computations overpredict the experimental results; however, trends are predicted reasonably well. The computed lateral-directional loads result from the asymmetric shock structures and vortices created by asymmetrically deflected canards. In addition, at high incidences, asymmetric crossflow shocks develop on the long afterbody between the canards and the tail, which produce body vortices that have a strong influence on the tail. Experimentally, asymmetric vortices are generated by the canards and shed from the afterbody as a consequence of boundary-layer separation.

Figure 13 illustrates computed pressure and axial vorticity contours at an axial station behind the canards ($z = 11$) and in front of the tail ($z = 30$) of Fig. 9. Solutions are shown for a missile orientation of 0 deg and angles of attack of 0, 10, and 18 deg. At 0-deg incidence, the asymmetric canard deflection induces circulation around the body which interacts with the tail. At 10-deg incidence, the vorticity created by the shocks on the canards moves away from the tail. At higher angles of

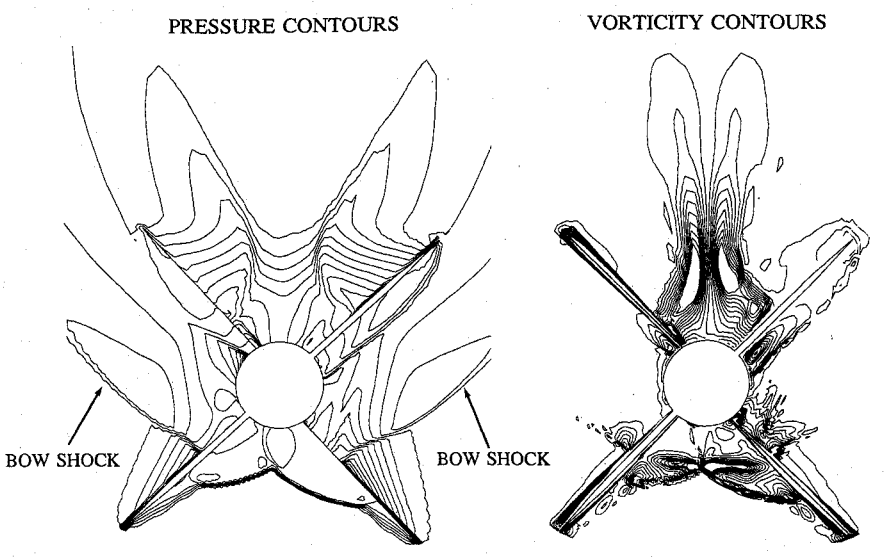

Fig. 8 Computed crossflow isobars and isovorticity contours for the configuration of Fig. 6 (looking downstream) with canards 2 and 4 deflected asymmetrically 10 deg for $\phi = 45$ deg at $M_\infty = 4.6$, $\alpha = 25$ deg, and $z = 29$.

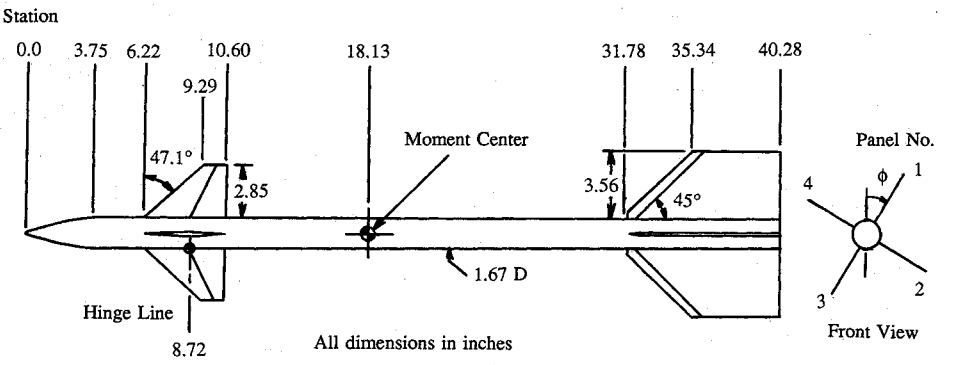

Fig. 9 Canard-body-tail configuration.[19]

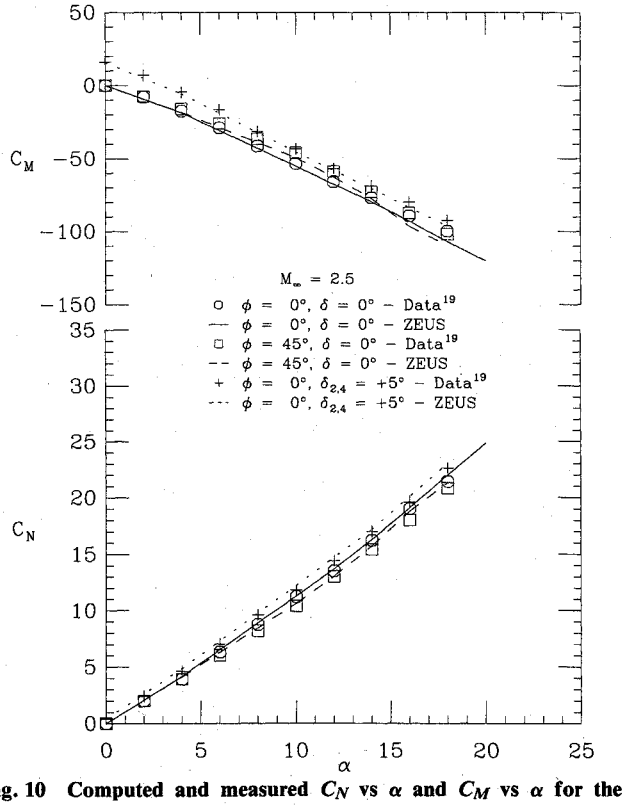

Fig. 10 Computed and measured C_N vs α and C_M vs α for the configuration of Fig. 10 at $M_\infty = 2.5$ for $\phi = 0$ and 45 deg without canard deflection and for $\phi = 0$ deg with the horizontal canards deflected + 5 deg.

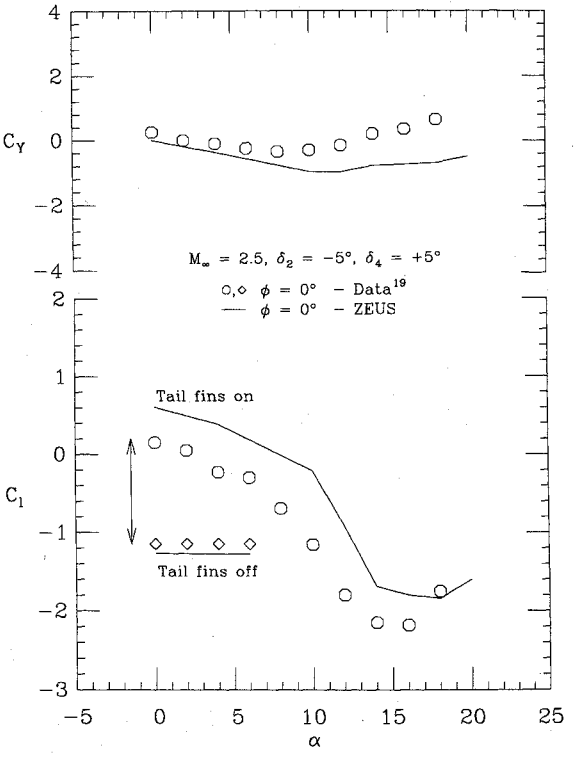

Fig. 11 Computed and measured C_l vs α and C_Y vs α for the configuration of Fig. 10 with canards 2 and 4 deflected asymmetrically 5 deg at $M_\infty = 2.5$ for $\phi = 0$ deg.

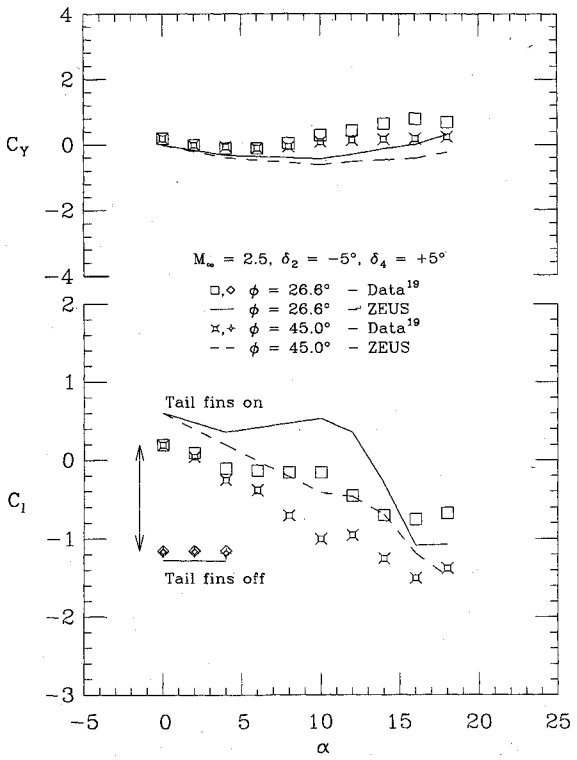

Fig. 12 Computed and measured C_l vs α and C_Y vs α for the configuration of Fig. 10 with canards 2 and 4 deflected asymmetrically 5 deg at $M_\infty = 2.5$ for $\phi = 26.6$ and 45 deg.

attack, crossflow shocks form on the leeside of the body, as illustrated for 18 deg incidence, which add vorticity into the flowfield in the vicinity of the tail, increasing the induced roll.

B. Discussion

The Euler equations can treat shocks of arbitrary strength and convect vorticity. The circulation produced by an Euler calculation on a missile is created by the bow shock, the fin leading edge shocks, and the crossflow shocks on the fin and the body. These calculations feature the appropriate fin vortices but generate body vortices through crossflow shocks. Experimentally observed body vortices, on the other hand, are a result of boundary-layer separation. Accounting for viscous phenomena, such as body vortices, is outside the scope of the Euler equations and must be accomplished through semiempirical modeling.

The tactical missile flowfield contains vortices that exert a significant and nonlinear influence on missile aerodynamics. Vortices are generated by forward lifting surfaces and body boundary-layer separation. Effective treatment of missiles requires the ability to predict the locations and strengths of the flowfield vortices.

Changes in incidence alter the vortex trajectories, as well as the number of vortices present, as is illustrated in Fig. 14 for a canard-body-tail missile. Three regimes exist for the canard/body vorticity interaction. At low angles of attack, only vortices from the deflected canards are present, and these impact the tail. At intermediate angles of attack, the canard vortices pass over the tail, and body vortices are still absent. At high incidence, the canard vortices move farther away from the body and the tail, while body vortices develop and interact with the tail. If the canards are deflected in opposite directions, asymmetries develop in the vortex structures that induce a side force and rolling moment on the tail.

The nonlinear variations in the C_l vs α curves of Figs. 7, 11, and 12 can be explained by considering the influence of such canard and afterbody vortices on the tail. For example, consider Fig. 11, in which the canards of Fig. 9 ($\phi = 0$ deg) are asymmetrically deflected 5 deg. At low incidences, different

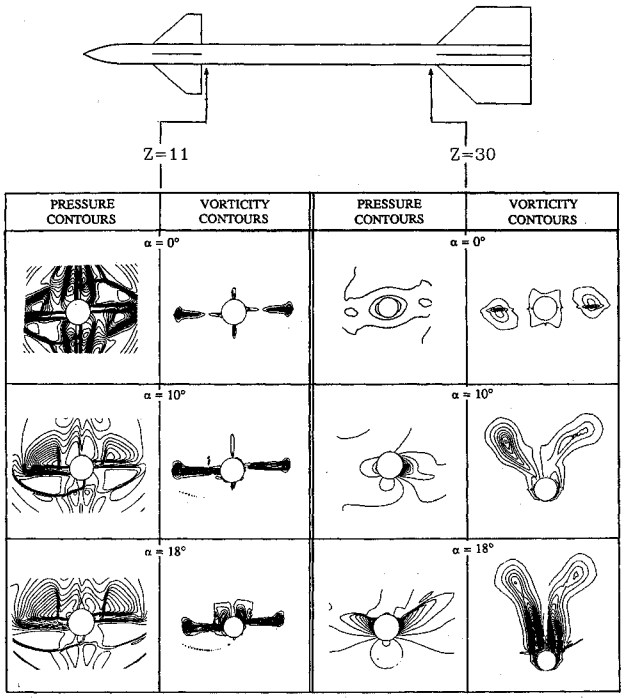

Fig. 13 Calculated crossflow isobars and isovorticity contours on the configuration of Fig. 10 (looking downstream) at $M_\infty = 2.5$ for $\phi = 0$ deg with the horizontal canards deflected asymmetrically 5 deg.

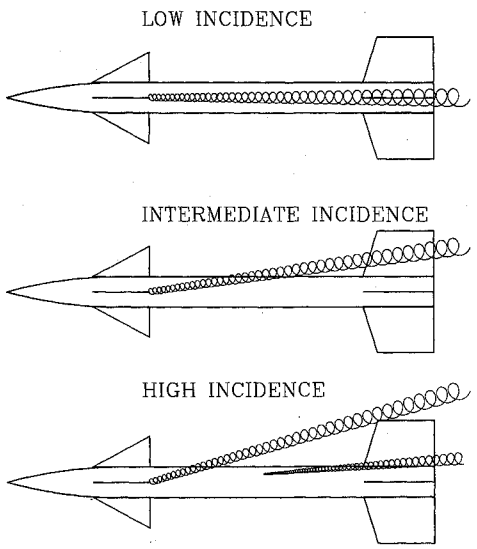

Fig. 14 Vortex structures in a tactical missile flowfield at different incidences.

rolling moments are obtained for the canard-body and the canard-body-tail configurations as indicated by the arrow. This variation can be attributed to the interaction of the asymmetric canard vortices with the tail. At intermediate incidences (5 deg $\leq \alpha \leq$ 12 deg), rolling moment for the canard-body-tail configuration diminishes to those of the canard-body shape. This is due to the canard vortices moving away from the body with increasing angle of attack. Increases in the rolling moment for the canard-body-tail configuration at higher incidences ($\alpha \geq 12$ deg) occur because of the interaction of asymmetric afterbody vortices, created computationally by asymmetric crossflow shocks, with the tail. Similar effects occur for $\phi = 26.6$ and 45 deg, as shown in Fig. 12.

IV. Concluding Remarks

It has been demonstrated that the ZEUS program is capable of predicting the nonlinear, vortex-induced, aerodynamic

characteristics of conventional missiles having canard control surfaces and a cruciform tail at supersonic Mach numbers. The computed longitudinal aerodynamic characteristics agree well with measured normal force and pitching moment, and the predicted lateral-directional aerodynamic characteristics follow the correct nonlinear trends.

The lack of quantitative agreement between calculated and measured lateral-directional aerodynamic characteristics can be traced to the inviscid model. Prediction of these quantities for a canard-body-tail configuration requires that the canard and body vortices be taken into account. Inviscid calculations feature the appropriate canard vortices, but body vortices are generated by crossflow shocks. By contrast, experimentally observed body vortices are a result of boundary-layer separation. The computed lateral loads exhibit the correct nonlinear trends with incidence. However, to obtain quantitative agreement with experiment, body vortices, generated by the appropriate mechanism, must be modeled in the calculation. This requires appending inviscid methods with an empirical model of boundary-layer separation.

Acknowledgments

This work was supported by the Naval Surface Warfare Center I. R. and the Naval Air Systems Command. The project monitor was Dale Hutchins (AIR-310-C).

References

[1]Hoeijmakers, H. W. M., "The Role of Computational Fluid Dynamics in Missile Aerodynamics," *Proceedings of the NEAR Conference on Missile Aerodynamics,* Oct. 1988, pp. 7.1-7.49.

[2]Moretti, G., Grossman, B., and Marconi, F., "A Complete Numerical Technique for the Calculation of Three-Dimensional Inviscid Supersonic Flow," AIAA Paper 72-192, 1972.

[3]Kutler, P., Reinhardt, W. A., and Warming, R. F., "Multishocked, Three-Dimensional Supersonic Flowfields with Real Gas Effects," *AIAA Journal,* Vol. 11, No. 5, 1973, pp. 657-664.

[4]Moretti, G., "Conformal Mappings for Computation of Steady, Three-Dimensional, Supersonic Flows," *Numerical/Laboratory Computer Methods in Fluid Dynamics,* American Society of Mechanical Engineers, New York, Vol. 13, 1976.

[5]Solomon, J. M., Ciment, M., Ferguson, R. E., and Bell, J. B., "Inviscid Flowfield Calculations for Reentry Vehicles with Control Surfaces," *AIAA Journal,* Vol. 15, No. 12, 1977, pp. 1742-1749.

[6]Wardlaw, A. B., Jr., Solomon, J. M., and Baltakis, F. P., "Supersonic Inviscid Flowfield Computations for Missile Type Bodies," *AIAA Journal,* Vol. 19, No. 7, 1981, pp. 899-906.

[7]Wardlaw, A. B., Jr., Baltakis, F. P., Solomon, J. M., and Hackerman, L. B., "An Inviscid Computational Method for Tactical Missile Configurations," Naval Surface Warfare Center, Silver Spring, MD, NSWC TR 81-457, Dec. 1981.

[8]Wardlaw, A. B., Jr., Priolo, F. J., and Baltakis, F. P., "Inviscid Multiple Zone Calculations for Supersonic Tactical Missiles," AIAA Paper 84-2099, Aug. 1984.

[9]Priolo, F. J., Wardlaw, A. B., Jr., Baltakis, F. P., and Solomon, J. M., "Inviscid Multiple Zone Strategy Applied to Complicated Supersonic Tactical Missile Configurations," AIAA Paper 85-1813, Aug. 1985.

[10]Wardlaw, A. B., Jr., Priolo, F. J., and Solomon, J. M., "A Multiple Zone Method for Supersonic Tactical Missiles," Naval Surface Warfare Center, Silver Spring, MD, NSWC TR 85-484, June 1986.

[11]Wardlaw, A. B., Jr., Baltakis, F. P., Martin, F. M., Priolo, F. J., and Jettmar, R. U., "Godunov's Method for Supersonic Tactical Missile Computations," *Journal of Spacecraft and Rockets,* Vol. 24, No. 1, 1987, pp. 40-47.

[12]Godunov, S. K., "A Finite Difference Method for the Numerical Computation of Discontinuous Solutions of the Equations of Fluid Dynamics," *Mat. Zb.,* Vol. 47, 1959, pp. 271-290.

[13]Wardlaw, A. B., Jr., and Davis, S. F., "A Second Order Godunov Method for Tactical Missiles," *AGARD, 58th Meeting of the Fluid Dynamic Panel Symposium on Applications of Computational Fluid Dynamics in Aeronautics,* April 1986.

[14]Wardlaw, A. B., Jr., and Davis, S. F., "A Second Order Godunov Method for Supersonic Tactical Missiles," Naval Surface Warfare Center, Silver Spring, MD, NSWC TR 86-506, Dec. 1986.

[15]Wardlaw, A. B., Jr., and Priolo, F. J., "Applying the ZEUS Code," Naval Surface Warfare Center, Silver Spring, MD, NSWC TR 86-508, Dec. 1986.

[16]Priolo, F. J., and Wardlaw, A. B., Jr., "Supersonic Non-Circular Missile Computations," AIAA Paper 88-0278; see also *Journal of Spacecraft and Rockets*, Vol. 26, No. 3, 1989, pp. 151-157.

[17]Lesieutre, D. J., Mendenhall, M. R., and Dillenius, F. E., "Prediction of Induced Roll on Conventional Missiles with Cruciform Fin Sections," AIAA Paper 88-0529, Jan. 1988.

[18]Monta, W. J., "Supersonic Aerodynamic Characteristics of a Sparrow III Type Missile Model With Wing Controls and Comparison With Existing Tail-Control Results," NASA TP 1078, Nov. 1977.

[19]Blair, A. B., Jr., Allen, J. M., and Hernandez, G., "Effect of Tail-Fin Span on Stability and Control Characteristics of a Canard-Controlled Missile at Supersonic Mach Numbers," NASA TP 2157, June 1983.

[20]Davis, S. F., "Simplified Second Order Godunov-Type Methods," *SIAM Journal on Scientific and Statistical Computing,* Vol. 9, May 1988, pp. 445-473.

Clark H. Lewis
Associate Editor